Supplement of Atmos. Chem. Phys., 25, 12483–12496, 2025
https://doi.org/10.5194/acp-25-12483-2025-supplement

Atmospheric Chemistry and Physics
Open Access

Supplement of

Cloud–radiation interactions amplify ozone pollution in a warming climate

Shuyu Zhao et al.

Correspondence to: Tian Feng (fengtian@nbu.edu.cn) and Minghu Ding (dingmh@cma.gov.cn)

Table S1 Model configurations. A detailed model information on the simulation domain, period, resolution, meteorological and chemical schemes, initial and boundary fields, and emission inventory. The spin-up time is 2 days.

Domain	
Period of baseline simulation	July, 2022
Size	200 grids × 200 grids
Center	120.0°E, 31.2°N
Horizontal resolution	6 km × 6 km
Vertical resolution	A flexible vertical interval, 35 vertical levels, spacing ranging from 50 m near the surface, 500 m at 2.5 km above the ground level, and more than 1 km above 14 km
Meteorology	
Microphysics scheme	WSM 6-class graupel microphysics scheme (Hong & Lim, 2006)
Boundary layer scheme	Mellor-Yamada-Janji planetary boundary layer scheme (Janjić, 2002)
Surface layer scheme	Monin-Obukhov surface layer scheme (Janjić, 2002)
Land-surface scheme	Noah land-surface model (Chen & Dudhia, 2001)
Longwave radiation scheme	Goddard (Dudhia, 1989)
Shortwave radiation scheme	Goddard (Dudhia, 1989)
Dry deposition	Wesely (1989)
Wet deposition	CMAQ by the U.S. EPA (Byun & Ching, 1999)
Chemistry	
Gas phase chemistry	SAPRC99 chemical mechanism (Binkowski and Roselle, 2003)
Inorganic aerosols	ISORROPIA version 1.7 (Nenes et al., 1998), SO_2 heterogeneous reaction on aerosol surface (G. Li et al., 2017)
Secondary organic aerosol	Non-traditional VBS parametrization (G. Li, Zavala, et al., 2011), NO_2 heterogeneous reaction (Li et al., 2010)
Photolysis rates	FTUV radiation transfer model (Tie et al., 2003; G. Li, Bei, et al., 2011)
Initial and boundary conditions	
Meteorological	NCEP FNL 6-h 1° × 1°
Chemical	CAM-chem 6-h outputs
Emission inventory	
Anthropogenic	MEIC (M. Li et al., 2017)
Biogenic	MEGAN (Guenther et al., 2006)

Table S2 Climate models and variables. A total of 41 models from CMIP6 are used, and each model name and variables therein are listed.

No.	Model name	T_max	TCC	SSRD
1	ACCESS-CM2	√	√	√
2	AWI-CM-1-1-MR	√	√	√
3	BCC-CSM2-MR	√	√	√
4	CAMS-CSM1-0	√	√	√
5	CanESM5	√	√	√
6	CanESM5-CanOE	×	√	√
7	CESM2	√	√	√
8	CESM2-WACCM	√	×	×
9	CIESM	×	×	√
10	CMCC-CM2-SR5	×	√	√
11	CMCC-ESM2	√	√	√
12	CNRM-CM6-1	√	√	√
13	CNRM-CM6-1-HR	√	√	√
14	CNRM-ESM2-1	√	√	√
15	E3SM-1-1	×	√	√
16	EC-Earth3	√	√	×
17	EC-Earth3-CC	√	√	√
18	EC-Earth3-Veg	√	√	×
19	EC-Earth3-Veg-LR	√	√	√
20	FGOALS-f3-L	×	×	√
21	FGOALS-g3	√	√	√
22	FIO-ESM-2-0	×	×	√
23	GFDL-ESM4	√	√	√
24	GISS-E2-1-G	×	√	√
25	HadGEM3-GC31-LL	×	√	√
26	HadGEM3-GC31-MM	×	√	√
27	IITM-ESM	×	√	√

28	INM-CM4-8	√	√	√
29	INM-CM5-0	√	√	√
30	IPSL-CM6A-LR	√	√	√
31	KACE-1-0-G	√	√	√
32	KIOST-ESM	√	√	√
33	MIROC6	√	√	√
34	MIROC-ES2L	√	√	√
35	MPI-ESM1-2-LR	√	√	√
36	MRI-ESM2-0	√	√	√
37	NESM3	√	√	√
38	NorESM2-LM	√	√	√
39	NorESM2-MM	√	√	√
40	UKESM1-0-LL	√	√	√
41	TaiESM1	×	√	√

Note: The number of models for projecting T_max, TCC, and SSRD varies significantly by the SSP, of which the number of models is the fewest under SSP1-1.9, with 12 models for T_max, 9 models for TCC, and 10 models for SSRD. Correspondingly, under SSP2-4.5, the number of models is 15, 31 and 33, respectively. Under SSP5-8.5, the number of models is 24, 34 and 37, respectively. "√" represents the variable is projected in the model, while "×" represents the variable is not projected.

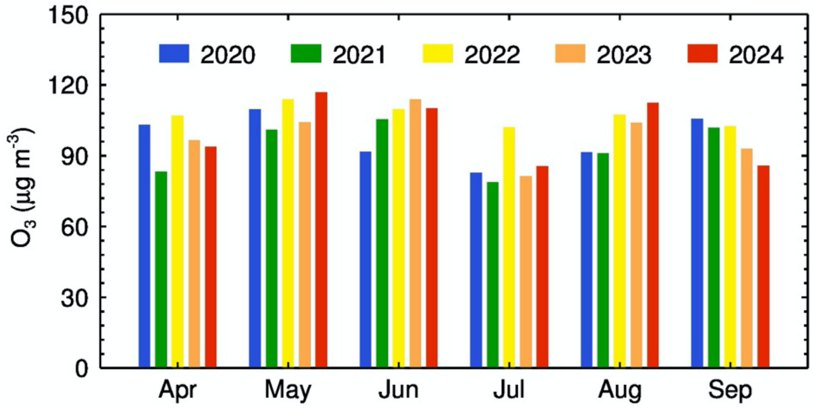

Figure S1 Warm-season O_3 variations. Interannual variation in monthly mean daytime (07:00-18:00, BJT) O_3 concentration from April to September during 2020-2024. Interannual variation in mean daytime O_3 concentration in July is highly consistent with the interannual variation in warm-season mean O_3 concentration, with the maximum in 2022.

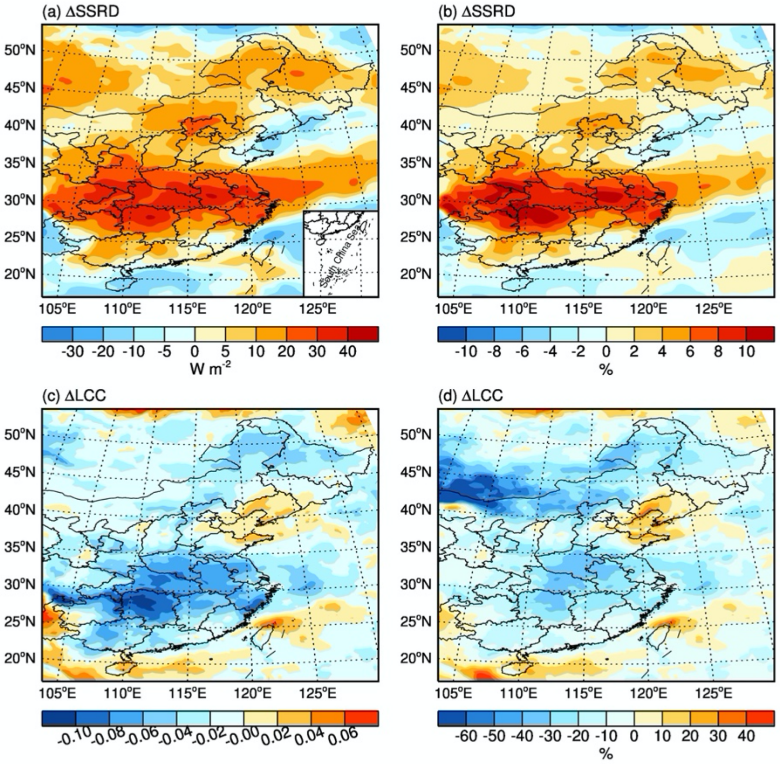

Figure S2 Observed anomaly in solar radiation for O_3 formation. (a) SSRD anomaly during the warm season of 2022 relative to the past decade (2014-2024). (b)Same as (a), but for the percentage change in SSRD. (c) LCC anomaly. (d) Same as (c), but for the relative percentage change in LCC. During the warm season of 2022, more SSRD and less LCC are observed in most of China, particularly in the region between 25°N and 35°N, where the YRD is located, with an anomalously more SSRD and less LCC. This is highly favorable for O_3 formation.

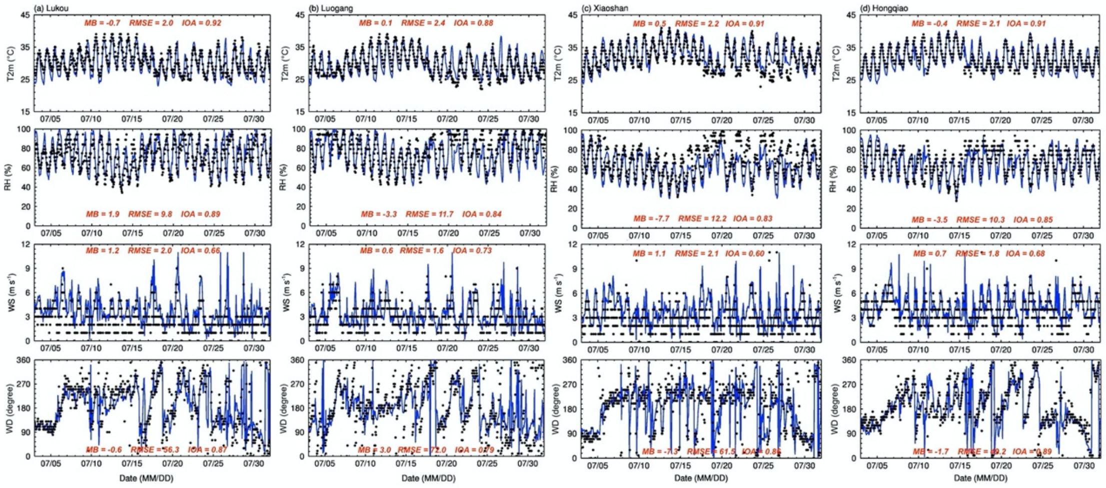

Figure S3 Observed and simulated meteorology for model performance. Observations data on T2m, RH, WS, and WD at four weather stations are from four international airports. (a) Lukou in Nanjing, Jiangsu. (b) Luogang in Hefei, Anhui. (c) Xiaoshan in Hangzhou, Zhejiang. (d) Hongqiao in Shanghai. The hourly simulations (blue curves) of four meteorological parameters are generally in good agreements with observations (black dots) at four airport weather stations in the YRD in July 2022. The MBs, RMSEs, and IOAs are shown in the margin.

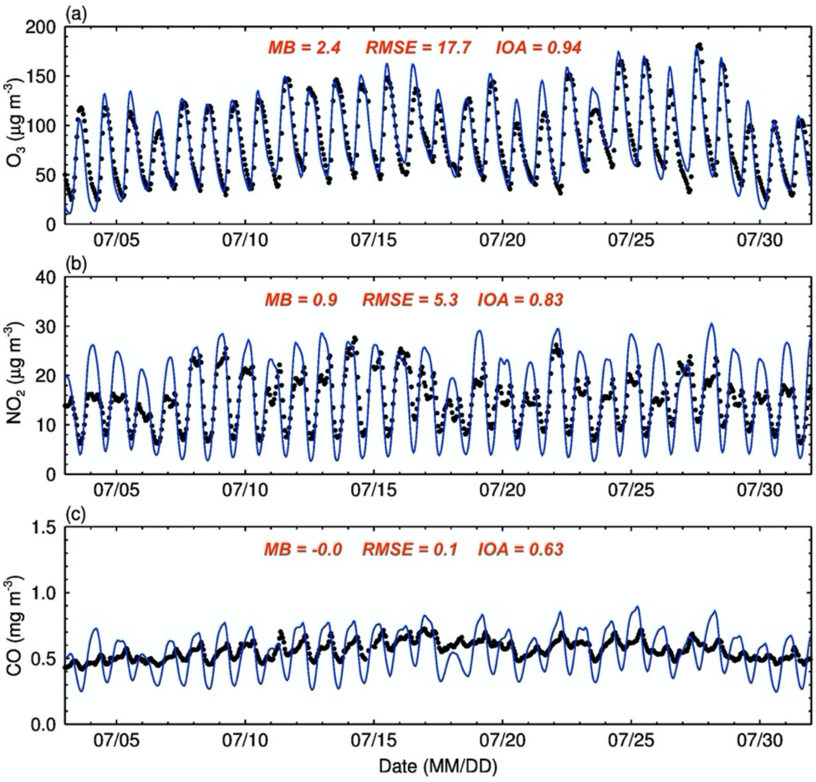

Figure S4 Model validation for pollutants. Comparison between observed (blue curves) and simulated (black dots) mass concentrations of pollutants. The model well reproduces temporal variations in O_3, NO_2, and CO in the YRD in July 2022. The MBs, RMSEs, and IOAs are shown in the top margin.

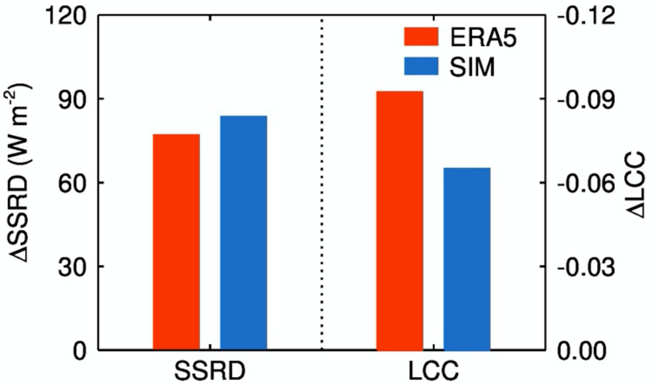

Figure S5 The simulated and observed interannual differences in SSRD and LCC. Differences in SSRD and LCC in July between 2021 and 2022 calculated by the model (the blue histograms) are highly closed to ECMWF ERA5 reanalysis data (the red histograms), showing a better performance of the model on the solar radiation change.

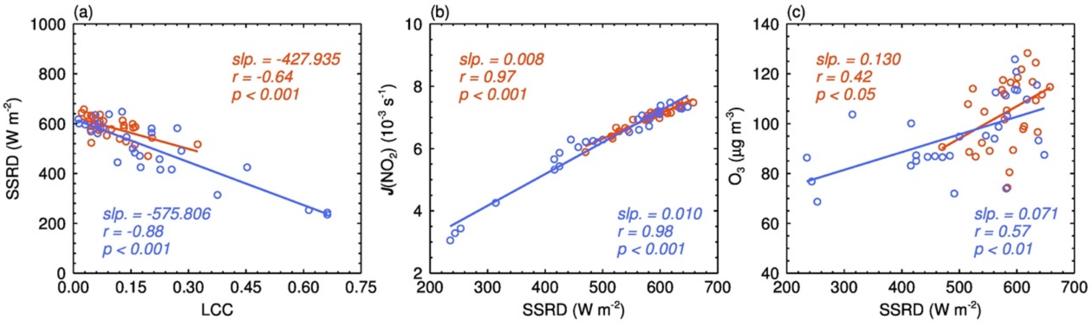

Figure S6 Simulated linkage between O_3 and LCC through SSRD. (a) A significantly negative correlation between SSRD and LCC, with confidence levels exceeding 99.9%. Consistent with observations in Figure 2a, SSRD is strongly modulated by the LCC. The more the LCC, the more SSRD is weakened. (b) The photolysis rates strongly depend on SSRD, and are mostly controlled by the SSRD, with the correlation coefficient highly close to 1.0, i.e., $r = 0.98$ (2021) and $r = 0.97$ (2022). For every 100 W m^{-2} increase in SSRD, the photolysis rate $J(NO_2)$ rises by 1.0×10^{-3} s^{-1}. (c) Relationship between O_3 and SSRD, O_3 concentration is significantly positively correlated with SSRD, with confidence levels exceeding 95%. The colored circles represent the simulations for July 2021 (blue) and July 2022 (red), respectively. The colored lines represent the linear fits corresponding to the circles of the same color.

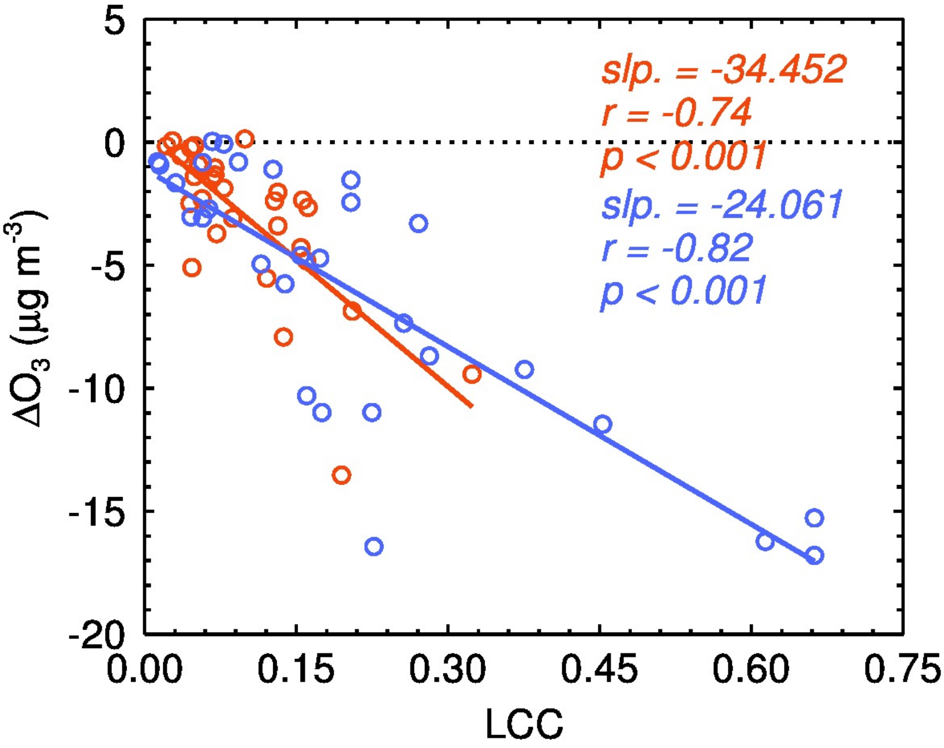

Figure S7 Same as Figure S6, but for relationship between ΔO_3 due to CRI and LCC. The ΔO_3 is significantly negatively correlated with LCC, with confidence levels exceeding 99.9%. The impact of LCC on ΔO_3 through CRI mechanism is more significant in the initial stage of clouds occurrence.

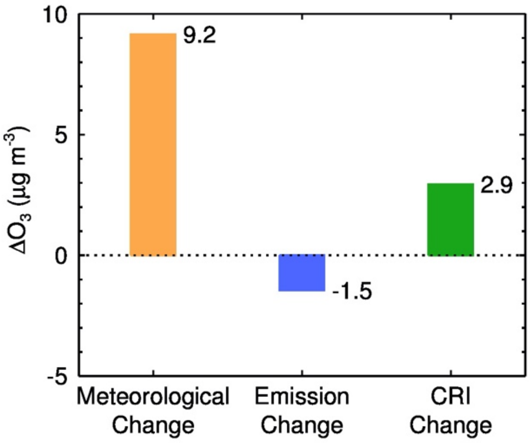

Figure S8 Contributions of interannual variability in various influence factors to ΔO_3. These factors include meteorological conditions, precursor emissions, and CRI. The changes in meteorological conditions also refer specifically to variabilities in LCC and SSRD.